

# Video-based Remote Physiological Measurement via Self-supervised Learning

Zijie Yue, Miaojing Shi, Shuai Ding

**Abstract**—Video-based remote physiological measurement aims to estimate remote photoplethysmography (rPPG) signals from human face videos and then measure multiple vital signs (e.g. heart rate, respiration frequency) from rPPG signals. Recent approaches achieve it by training deep neural networks, which normally require abundant face videos and synchronously recorded photoplethysmography (PPG) signals for supervision. However, the collection of these annotated corpora is uneasy in practice. In this paper, we introduce a novel frequency-inspired self-supervised framework that learns to estimate rPPG signals from face videos without the need of ground truth PPG signals. Given a video sample, we first augment it into multiple positive/negative samples which contain similar/dissimilar signal frequencies to the original one. Specifically, positive samples are generated using spatial augmentation. Negative samples are generated via a learnable frequency augmentation module, which performs non-linear signal frequency transformation on the input without excessively changing its visual appearance. Next, we introduce a local rPPG expert aggregation module to estimate rPPG signals from augmented samples. It encodes complementary pulsation information from different face regions and aggregate them into one rPPG prediction. Finally, we propose a series of frequency-inspired losses, *i.e.* frequency contrastive loss, frequency ratio consistency loss, and cross-video frequency agreement loss, for the optimization of estimated rPPG signals from multiple augmented video samples and across temporally neighboring video samples. We conduct rPPG-based heart rate, heart rate variability and respiration frequency estimation on four standard benchmarks. The experimental results demonstrate that our method improves the state of the art by a large margin. Our codes will be available at <https://github.com/yuezijie/Video-based-Remote-Physiological-Measurement-via-Self-supervised-Learning>.

**Index Terms**—Remote physiological measurement, self-supervised learning, frequency augmentation, local rPPG expert, frequency-inspired losses.

## 1 INTRODUCTION

PHYSIOLOGICAL signals, such as heart rate (HR), heart rate variability (HRV) and respiration frequency (RF), are important vital signs to reflect human health status. Medical equipments like electrocardiography (ECG) and photoplethysmography (PPG) recording devices can measure these signals in a skin-contact way. However, skin-contact electrodes and wires often cause inconvenience and discomfort to users, sometimes lead to allergic reactions [1], [2], [3]. Recently, there is a growing interest in measuring physiological signals from human face videos captured by RGB cameras [4], [5], [6]. This remote physiological measurement has been used in a number of applications, such as atrial fibrillation screening [7], [8] and driver status assessment [9].

Most remote physiological measurement approaches are based on the remote photoplethysmography (rPPG) principle [10], *i.e.* the optical absorption of skins changes periodically along with the periodic change of blood volume. Ideally, the change of skin color over time reflects the periodic rPPG signal and can be used to measure physiological signs including HR, HRV and RF. Nevertheless, periodic rPPG signals are easily affected by non-periodic noises, which can be caused by illumination changes, facial expressions and head movements [5], [11]. Traditional approaches pro-

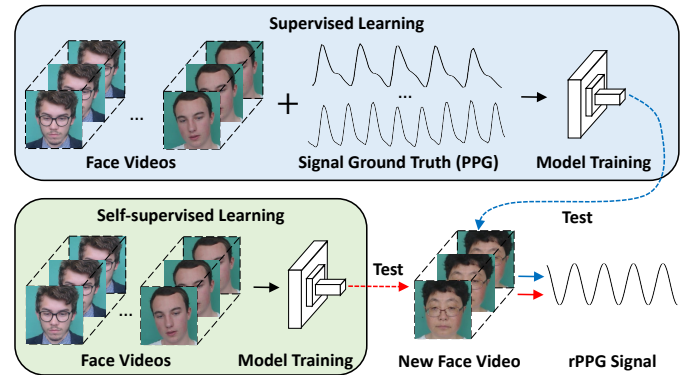


Fig. 1. Modern remote physiological measurement approaches train DNNs to estimate rPPG signals from face videos. Supervised methods require signal ground truth recorded synchronously with face videos for model training. While our self-supervised method trains the model from unlabelled face videos without pre-recorded PPG signals.

pose blind signal separation techniques [12], [13] and skin reflection models [10], [14] to separate rPPG signals from noises. These approaches rely on prior assumptions, *e.g.* the normalized skin tone is the same for different people under white light [14], which can not always satisfy, hence leading to the performance degradation [15], [16].

With the advent of deep learning [17], modern remote physiological measurement approaches train deep neural networks (DNNs) to estimate rPPG signals from face videos [1], [2], [4], [5], [15], [16], [18]. These methods are trained in a supervised manner, where PPG signals are recorded

- Z. Yue and S. Ding are with the School of Management, Hefei University of Technology, China. (e-mail: zijie.yue@kcl.ac.uk; ding-shuai@hfut.edu.cn).
- M. Shi is with the Department of Informatics, King's College London, UK. (e-mail: miaojing.shi@kcl.ac.uk).

synchronously with face videos for supervision [1], [2], [4], [5], [15], [16], [18] (see Fig. 1). The collection of these annotated corpora is however not easy: subjects must wear skin-contact devices and keep body still to record both signals and videos. To bypass this process, Gideon *et al.* [19] has tried to train a rPPG estimator based on unlabeled data using contrastive learning. Given an input video, they re-sample it with a pre-defined ratio to its negative counterpart, which has a different rPPG signal frequency. rPPG signals are estimated from both the input and resampled videos. The contrastive loss is applied among these signals for model optimization. [19] is the first DNN-based self-supervised work for rPPG estimation. It generates only one negative sample with a higher rPPG signal frequency to that of the input, which limits the sample diversity and can lead to inferior model generalizability.

In this paper, we propose a novel frequency-inspired self-supervised framework for video-based remote physiological measurement, which learns to optimize rPPG estimations from multiple augmented videos of different signal frequencies and across temporally neighboring videos of similar signal frequencies. It has three main stages: data augmentation, signal extraction and network optimization. Given an input video, *in the first stage*, we apply spatial augmentation (*e.g.* image rotation and flip) to obtain multiple positive samples, which contain rPPG signals with the same frequency to that of the input. Meanwhile, we design a learnable frequency augmentation (LFA) module to generate multiple negative samples which contain rPPG signals with different frequencies to that of the input. Unlike [19], our LFA module is integrated into the DNN for end-to-end training and produces multiple samples with controllable rPPG signal frequencies, which can be higher or lower than that of the input. *In the second stage*, because face is not an ideal Lambertian object, the distribution of blood vessel or noise varies over different regions in a face. Instead of treating face regions indiscriminately [3], [19], we design a local rPPG expert aggregation (REA) module to estimate rPPG signals from different face regions and aggregate them via a spatio-temporal gating net. The REA module is respectively devised for each augmented video sample (positive or negative) to obtain its rPPG signal. *In the third stage*, since we do not have ground truth PPG signals, we first introduce a frequency contrastive loss and a frequency ratio consistency loss to optimize our estimated rPPG signals. Furthermore, since the frequency of rPPG signal does not change rapidly over a short term, we additionally extract rPPG signals from multiple temporally neighboring videos to the input and introduce a cross-video frequency agreement loss for rPPG estimation across videos.

Overall, our new frequency-inspired self-supervised framework for remote physiological measurement has three key contributions:

- 1) We design a learnable frequency augmentation module to generate sufficient and diverse negative samples for self-supervised learning.
- 2) We introduce a local rPPG expert aggregation module to learn complementary information from different face regions for rPPG estimation.
- 3) We propose a series of frequency-inspired losses

(*i.e.* frequency contrastive loss, frequency ratio consistency loss, cross-video frequency agreement loss) for the optimization of rPPG signals extracted from the input’s augmentations and neighbors.

We conduct extensive experiments on four standard benchmarks, *i.e.* UBFC-rPPG [20], PURE [21], DEAP [22], and MMVS [3]. Results show our approach significantly outperforms the state of the art self-supervised method and performs on par with state of the art supervised methods.

## 2 RELATED WORK

### 2.1 Remote physiological measurement

Video-based remote physiological measurement has been mainly implemented using blind signal separation [12], [23], skin reflection models [10], [14], and deep neural networks [1], [4], [15]. Blind signal separation-based approaches assume that the skin color change is a linear combination of the target rPPG signal and other noises. They use signal decomposition methods, such as independent component analysis or principal components analysis, to separate rPPG signals from noises. For example, Macwan *et al.* [24] used auto-correlation as a measurement for signal periodicity, so as to guide independent component analysis for rPPG signal separation. Skin reflection model-based approaches explore different ways to project images from the RGB space to other color spaces for better rPPG estimation. For instance, Haan *et al.* [14] proposed to project images into the chrominance space to eliminate motion noises and help rPPG estimation. These approaches rely on assumptions, for instance, different people’s skin tones are identical under white light [14], which may not always satisfy in a practical environment [15], [16].

Recently, DNN-based approaches have shown superior performance on remote physiological measurement [1], [2], [3], [5], [16], [18], [25]. Hu *et al.* [26] designed a time-domain attention network to extract and aggregate temporal information from multiple video segments for rPPG estimation. Song *et al.* [15] transformed the chrominance signals in [14] into accurate rPPG wave forms using a conditional generative adversarial network. Yu *et al.* [18] and Yue *et al.* [3] respectively addressed rPPG estimation from highly compressed and low-resolution face videos by adding video enhancement networks. Yu *et al.* [25] used transformer blocks to model the relationship among video frame features. Despite the remarkable achievements in these approaches, they need abundant videos with synchronously recorded PPG signals for training. The collection of these annotated corpora is however uneasy. Gideon *et al.* [19] tackled this by training the DNN in a self-supervised manner using unlabelled data: they resampled the input video to create its negative counterpart and apply a contrastive loss among rPPG signals extracted from the input and resampled videos.

We propose a new frequency-inspired self-supervised framework for video-based remote physiological measurement. It differs from [19] significantly: 1) for data augmentation, [19] uses pre-processed video re-sampling to generate one negative sample, whose rPPG signal frequency can only be higher than that of the original sample. Our LEA module

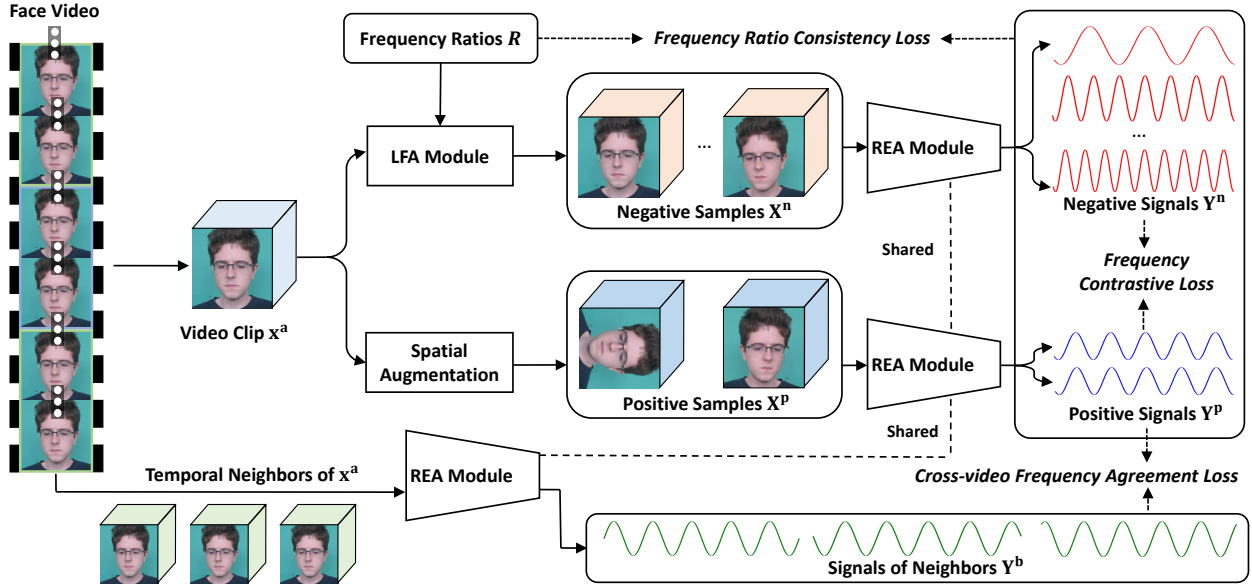


Fig. 2. The overall architecture of our framework. It comprises of three main stages. 1) Data augmentation: we randomly select a video clip from a short face video as input while keep other clips as the input’s neighbors for later usage. We respectively apply spatial augmentation and learnable frequency augmentation (LFA) on the input to generate positive and negative video samples. 2) Signal extraction: we design the local rPPG expert aggregation (REA) module to extract rPPG signals from positive/negative video samples. 3) Model optimization: we develop a series of frequency-inspired losses, *i.e.* frequency contrastive loss, frequency ratio consistency loss, cross-video frequency agreement loss, for the optimization of rPPG signals generated from the input video’s augmentations and temporal neighbors.

is instead learned to augment samples with arbitrary signal frequencies. 2) for signal extraction, in [19], it only captures image-level features and treats different face regions indiscriminately. Our REA module instead considers the pulsatile feature variance over face regions and advantageously aggregates their information for rPPG estimation; 3) for model optimization, [19] applies the contrastive loss among anchor, positive and negative rPPG signals. They all come from one video clip. We design a series of frequency-inspired losses; especially, the cross-video frequency agreement loss is among rPPG signals extracted from multiple video clips.

It is worth of noting that the three key contributions of our self-supervised framework are also unique among supervised methods in the remote physiological measurement.

## 2.2 Self-supervised learning

Self-supervised learning aims to learn an effective data embedding function from unlabelled data during training. Previous works focus on designing different pretext tasks to train the data encoders. For image encoders, solving jigsaw puzzles [27], rotation prediction [28] and counting primitives [29] are widely used tasks. For video encoders, predicting frames [30] and tracking patches [31] can help them learn useful feature representations. Recently, contrastive self-supervised learning attracts much attention and shows promising performance compared to supervised learning [32], [33], [34], [35], [36], [37]. Owing to the versatile data augmentation techniques, contrastive learning approaches augment the input into multiple positive counterparts, while consider other samples from different classes as negatives to the input. They minimize feature distances between positive sample pairs while maximizing feature distances between negative sample pairs. For instance, SimCLR [34] leverages image cropping, color distortions

and blurring to augment the input and apply contrastive learning. Dangovski *et al.* [38] proposed the equivariant contrastive learning, which utilizes an additional branch to predict the adopted augmentations of positive samples. Qian *et al.* [39] designed a novel temporal augmentation method for video representation learning, which samples non-overlapping positive video clips from the original video using different temporal intervals. Pan *et al.* [40] introduced another temporal augmentation method which obtains positive videos using a generate adversarial network. The network removes several frames from a given video while maintaining its spatio-temporal information. Unlike above approaches that use spatial or temporal augmentation, we need to generate samples that contain different frequencies of rPPG signals. Hence, we propose a learnable frequency augmentation module.

## 2.3 Mixture of experts

Mixture of experts (MoE) divides a complex task into multiple sub-tasks and distributes them amongst multiple experts in a model [41], [42]. A gating net is devised to assign soft or hard weights to experts to control their activations [41]. Recently, MoE-based deep learning approaches have shown superior performance in many fields, such as image super-resolution [43], multi-modal/task learning [44], [45], and medical imaging [46]. For instance, Ma *et al.* [45] proposed a multi-gate MoE for multi-task learning. Experts capture task-shared representations while gating nets combine them using task-specific weights. Sahasrabudhe *et al.* [46] extracted information from blood smear images and patient clinical attributes (*e.g.* age and lymphocyte count) using a CNN and MLP model, respectively; they combined the outputs of two models via a gating net for the diagnosis of lymphocytosis. We for the first time leverage multiple

experts to estimate rPPG signals in different face regions and aggregate their complementary information via a spatio-temporal gating net.

### 3 METHOD

#### 3.1 Overview

Our goal is to learn rPPG signals from unlabelled face videos. The overview of our framework is illustrated in Fig. 2. The basic pipeline is to first generate positive and negative samples from the input video, then extract rPPG signals from them, and finally learn contrastive frequency information among these rPPG signals. Specifically, given a short face video, we cut it into several clips, each with  $T$  frames. One clip is randomly selected as the main input  $\mathbf{x}^a$  while the rest is taken as  $\mathbf{x}^a$ 's temporal neighbors for later usage. In the data augmentation stage (Sec. 3.2), we first apply spatial augmentation to  $\mathbf{x}^a$ , which does not affect its interior rPPG signals, to generate a number of positive samples  $\mathbf{X}^p = \{\mathbf{x}^p\}$ . Next, we introduce the learnable frequency augmentation (LFA) module to generate a number of negative samples  $\mathbf{X}^n = \{\mathbf{x}^n\}$  which have different rPPG signal frequencies to that of  $\mathbf{x}^a$ . We feed a set of frequency ratios  $R = \{r\}$  into the LFA module to modulate the rPPG signal of  $\mathbf{x}^a$ . Having  $\mathbf{X}^p$  and  $\mathbf{X}^n$ , in the signal extraction stage (Sec. 3.3), we pass them into local rPPG expert aggregation (REA) modules to estimate corresponding rPPG signals, denoted by  $\mathbf{Y}^p = \{\mathbf{y}^p\}$  and  $\mathbf{Y}^n = \{\mathbf{y}^n\}$  respectively. The REA module encodes complementary pulsation information from different face regions and uses a spatio-temporal gating net to aggregate the information for a final rPPG prediction. Last, in the network optimization stage (Sec. 3.4), the frequency contrastive loss is applied among signals from  $\mathbf{Y}^p$  or between  $\mathbf{Y}^p$  and  $\mathbf{Y}^n$ . The frequency ratio consistency loss is applied between signals from  $\mathbf{Y}^p$  and  $\mathbf{Y}^n$  to enforce their frequency ratios according to input ratios in  $R$ . We also introduce a cross-video frequency agreement loss by extracting rPPG signals from  $\mathbf{x}^a$ 's temporal neighbors and enforce their frequencies to be similar to that of  $\mathbf{x}^a$ .

#### 3.2 Data augmentation: learnable frequency augmentation

Given the input video  $\mathbf{x}^a$ , we apply two different data augmentation strategies to generate positive and negative samples, respectively. For positive ones, we employ six weakly spatial augmentation operations, *i.e.* image rotations ( $0^\circ$ ,  $90^\circ$ ,  $180^\circ$ , and  $270^\circ$ ), horizontal and vertical flips. They do not affect the interior rPPG signal of  $\mathbf{x}^a$ . Every time, we randomly select two operations to apply to  $\mathbf{x}^a$  and obtain two positive samples  $\tilde{\mathbf{X}}^p = \{\mathbf{x}_1^p, \mathbf{x}_2^p\}$ . They have the same rPPG signal frequency to that ( $f^a$ ) of  $\mathbf{x}^a$ .

Next, we design a learnable frequency augmentation (LFA) module to generate multiple negative samples which contain rPPG signals with different frequencies to that of  $\mathbf{x}^a$ . Given the input of  $\mathbf{x}^a$  and a frequency ratio  $r_i$ , it has a *pyramid* structure (see Fig. 3) to transform  $\mathbf{x}^a$  to a new sample  $\mathbf{x}_i^n$  with its rPPG signal frequency becoming  $r_i \times f^a$ . In the structure, we first use one 3D Convolution (Conv) layer followed by two 3D Res-blocks (3D RB) to extract the feature for  $\mathbf{x}^a$  and then down sample it with

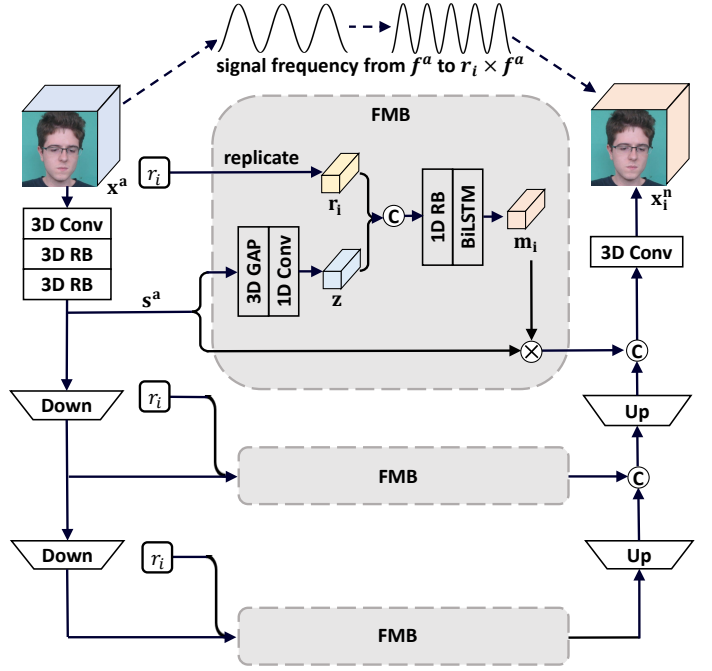


Fig. 3. Illustration of the LFA module. It performs frequency modulation on multi-scale features of the input video  $\mathbf{x}^a$ . The core of LFA module is the frequency modulation block (FMB), which produces the frequency modulation vector given the input scale feature  $s^a$  and the frequency modulation ratio  $r_i$ . The frequency modulation vector is multiplied back to  $s^a$  to change its rPPG signal frequency. Finally we aggregate multi-scale outputs to obtain the negative video sample  $\mathbf{x}_i^n$ .

a factor of 2 and 4 to obtain the multi-scale features. These features reflect different levels of details for  $\mathbf{x}^a$ . We modulate the frequency of rPPG signal on each scale via the frequency modulation block (FMB, see below Sec. 3.2.1). The modulated features are upsampled and concatenated. We reconstruct the video clip from the concatenated feature via one 3D Conv ( $1 \times 1 \times 1$ ). The reconstructed video clip is denoted by  $\mathbf{x}_i^n$  and is regarded as a negative sample to  $\mathbf{x}^a$ .

We know the frequency of human rPPG signal varies within a rather small range as a result of the limit for human normal heart rate. On one hand, we need to reinforce the module to change the rPPG signal frequency of  $\mathbf{x}^a$  to the target. On the other hand, we also make sure there is no excessive color difference between  $\mathbf{x}^a$  and  $\mathbf{x}_i^n$  to avoid significant frequency change. We therefore develop the frequency ratio consistency loss (specified later in Sec. 3.4.2) and video reconstruction loss (see below Sec. 3.2.2) for the two purposes, respectively. Overall, we randomly sample a set of frequency ratios  $R = \{r_1, \dots, r_k\}$  within a range of  $(0.3, 0.8) \cup (1.2, 1.7)$  and feed them into the LFA module to augment  $k$  negative samples  $\mathbf{X}^n = \{\mathbf{x}_1^n, \dots, \mathbf{x}_k^n\}$  to  $\mathbf{x}^a$ , which contain rPPG signals with frequencies of  $\{r_1 f^a, \dots, r_k f^a\}$ .

##### 3.2.1 Frequency modulation block

The FMB, as illustrated in Fig. 3, takes the input of a certain scale feature  $s^a \in \mathbb{R}^{T \times H \times W \times C}$  and frequency ratio  $r_i$  (scalar).  $s^a$  is passed through a 3D global average pooling (3D GAP) to collapse its spatial dimensions and then a 1D Conv to collapse its channel dimension, so as to obtain a rough rPPG signal  $\mathbf{z} \in \mathbb{R}^{1 \times T}$ . We aim to change the



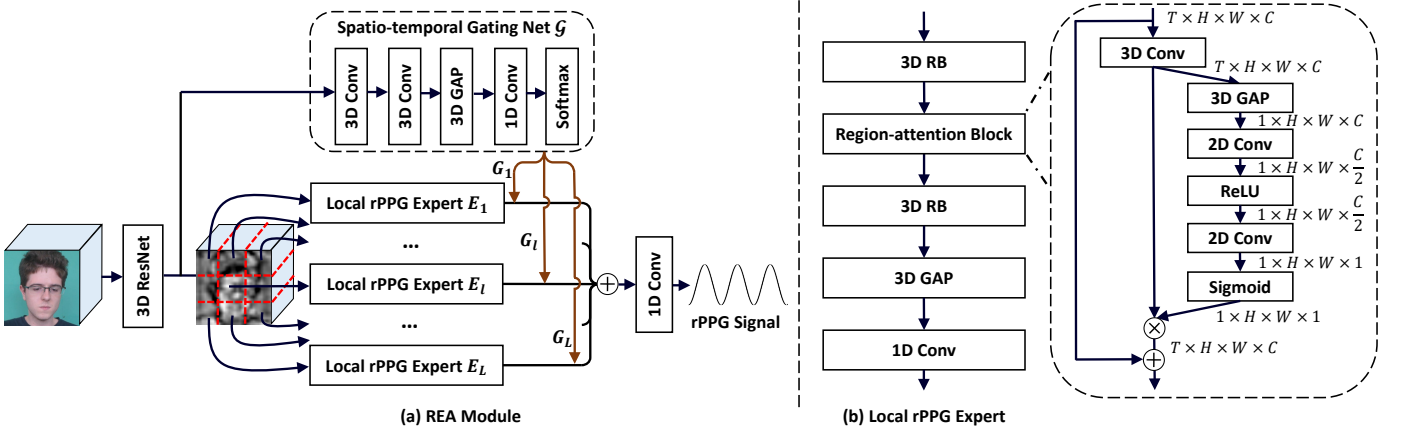


Fig. 4. (a) The local rPPG expert aggregation (REA) module captures complementary pulsation information from different face regions. We regard the rPPG estimation from each local region as a local rPPG expert. Different experts are aggregated through a spatio-temporal gating net. (b) The structure for obtaining one local rPPG expert.

frequency of  $\mathbf{z}$  from  $f^a$  to  $r_i \times f^a$ . Directly multiplying  $\mathbf{z}$  by  $r_i$  only changes the signal amplitude but not frequency. In practice, we replicate  $r_i$  to the length of  $T$  and concatenate it with  $\mathbf{z}$ . Their concatenation is processed via a 1D RB and a Bidirectional LSTM (BiLSTM). The Conv + ReLu in the 1D RB performs local transformation on the signal while the BiLSTM performs global transformation on it. This outputs a modulation vector  $\mathbf{m}_i \in \mathbb{R}^{1 \times T}$ , each of its entries can be seen as a multiplier to the corresponding component in  $\mathbf{z}$ , or equivalently corresponding frame in  $\mathbf{s}^a$ . We element-wisely multiply  $\mathbf{m}_i$  to  $\mathbf{s}^a$  to change its rPPG signal frequency from  $f^a$  to  $r_i \times f^a$ . Note that, to obtain  $\mathbf{m}_i$  from the concatenation of  $\mathbf{r}_i$  and  $\mathbf{z}$ , the transformation needs to be non-linear (*i.e.* 1D RB and BiLSTM). This is due to the nature of signal frequency modulation. We give an example: assuming we have a periodic signal,  $\alpha = A \sin(2\pi F(t + \varphi))$ , where  $A$ ,  $F$  and  $\varphi$  denotes the signal amplitude, frequency and shift, respectively. To modulate its frequency by a factor of 2, *i.e.* obtaining  $\beta = A \sin(4\pi F(t + \varphi))$ , we can compute the modulation vector as  $\beta/\alpha = 2 \cos(2\pi F(t + \varphi))$ , which indicates a non-linear transformation.

### 3.2.2 Video reconstruction loss

To prevent the excessive color difference between  $\mathbf{x}^a$  and  $\mathbf{x}_i^n$ , we can regulate either their modulation weight  $\|\mathbf{m}_i - 1\|_2$  or pixel-wise color distance to be small. The latter works empirically better than the former in our experiment (Sec. 4.4.4). We conceptualize the latter as the video reconstruction loss  $\mathcal{L}_{vr}$ , which is indeed widely used in video frame inpainting [47] and video super-resolution [48], and write it out:

$$\mathcal{L}_{vr} = \frac{1}{k} \sum_{i=1}^k \|\mathbf{x}_i^n - \mathbf{x}^a\|_2 \quad (1)$$

This loss enforces the LFA module to augment negative samples which retain the general visual appearance of  $\mathbf{x}^a$ .

## 3.3 Signal extraction: local rPPG expert aggregation

We extract the rPPG signal from each augmented sample via the local rPPG expert aggregation (REA) module. Our motivation is that different face regions have varying distributions of blood vessels and noises and should contribute differently to the rPPG estimation. Our REA module is

designed to combine complementary pulsation information from these regions for an accurate rPPG estimation.

The structure of the module is illustrated in Fig. 4a. We first leverage the 3D ResNet-10 [3] to encode the input video into a feature tensor. The feature tensor is then divided into  $L$  evenly partitioned regions where we extract rPPG signal from each of them and denote it as a local rPPG expert  $E_i$ . As illustrated in Fig. 4b,  $E_i$  is obtained via two 3D RBs for feature processing; one region-attention block in-between the two 3D RBs for capturing physiological clues from pulsation-sensitive skins; and one 3D GAP followed by one 1D Conv for projecting the feature into 1D signal. Having  $E_1, E_2, \dots, E_L$  for  $L$  regions, we design a spatio-temporal gating net  $\mathcal{G}$  to aggregate different experts into one rPPG prediction. Below we specify our region-attention block and spatio-temporal gating net.

### 3.3.1 Region-attention block

Within each face region, some pixels may belong to background that do not contribute to rPPG estimation; while some other pixels, despite on the face, are insensitive to blood pulsation (*e.g.* eyes and mouth). Region-attention block is thereby introduced to focus rPPG estimation on the pulsation-sensitive skin area. Fig. 4b illustrates its structure: given the 4D input feature tensor ( $\mathbb{R}^{T \times H \times W \times C}$ ), after a 3D Conv, we leverage a 3D GAP to collapse it along the temporal dimension into a 3D tensor ( $\mathbb{R}^{1 \times H \times W \times C}$ ). Inspired by the squeeze and excitation operation in [49], we then pass the feature into consecutive 2D Conv and non-linear activation layers (*i.e.* ReLu, Sigmoid) for aggregating information across the channel dimension and obtaining the region-attention map. The attention map is pixel-wisely multiplied to the input 4D feature. A skip connection is also leveraged to retain the input information. Our scheme indeed transforms the image-based channel-wise attention in [49] into video-based spatial-wise attention, which enhances the pulsation-sensitive area while suppresses background and pulsation-insensitive area in rPPG estimation.

### 3.3.2 Spatio-temporal gating net

The idea of employing a gating net to combine experts is from mixture of experts [41]. The conventional de-

sign of gating net [43], [46] normally assigns sample-level weights among experts. Unlike them, we introduce the spatio-temporal gating net  $\mathcal{G}$  which assigns spatio-temporal weights to combine temporal rPPG signals (experts) extracted from different spatial regions. Our motivation is that some regions may reflect rPPG signal better during the systole while some are more sensitive during the diastole. Each expert signal should be assigned with different weights at different moments. The structure of  $\mathcal{G}$  is hence illustrated in Fig. 4a, consisting of two 3D Convs followed by a 3D GAP, a 1D Conv and a Softmax layer. The gating net generates  $L$  vectors,  $G_1, G_2, \dots, G_L$ , corresponding to  $L$  spatial regions. Each vector is of dimension  $1 \times T$ , equivalent to the temporal dimension of each expert. Vector components of the same index are softmaxed across experts. We elementwisely multiply each  $G_l$  to its corresponding  $E_l$  and obtain the final rPPG signal as a weighted combination:

$$\mathbf{y} = \sum_{l=1}^L E_l \cdot G_l \quad (2)$$

The REA module is devised to positive and negative video samples to produce positive signals  $\mathbf{Y}^p = \{\mathbf{y}_1^p, \mathbf{y}_2^p\}$  and negative signals  $\mathbf{Y}^n = \{\mathbf{y}_1^n, \mathbf{y}_2^n, \dots, \mathbf{y}_k^n\}$ . These signals are of various frequencies and can be used for subsequent self-supervised training.

### 3.4 Network optimization: frequency-inspired losses

We introduce a series of frequency-inspired losses, *i.e.* frequency contrastive loss, frequency ratio consistency loss, cross-video frequency agreement loss, for the optimization of rPPG signals generated from the input video’s augmentations and neighbors.

#### 3.4.1 Frequency contrastive loss

Since we do not have ground truth PPG signals for training, we use the popular contrastive self-supervised learning [32], [50] to pull close rPPG signals ( $\mathbf{Y}^p = \{\mathbf{y}^p\}$ ) from positive samples while push them away from rPPG signals ( $\mathbf{Y}^n = \{\mathbf{y}^n\}$ ) from negative samples in the feature space. We adapt the InfoNCE loss [50] to write out our frequency contrastive loss  $\mathcal{L}_{fc}$ :

$$\mathcal{L}_{fc} = \log\left(\frac{\exp(d(\mathbf{y}_1^p, \mathbf{y}_2^p)/\tau)}{\sum_{i=1}^k (\exp(d(\mathbf{y}_1^p, \mathbf{y}_i^n)/\tau) + \exp(d(\mathbf{y}_2^p, \mathbf{y}_i^n)/\tau))} + 1\right) \quad (3)$$

where  $d(\cdot, \cdot)$  measures frequency difference between two signals and  $\tau$  is the temperature. We follow [19] to realize  $d$  as the mean squared error between power spectral densities (PSD) of two signals; PSD describes the power of different frequency components in a signal. Notice [19] utilizes the triplet loss to optimize among only three signals, *i.e.* anchor, positive and negative; we have a different loss form to [19] as a result of our larger numbers of positive and negative signals generated by different ways.

#### 3.4.2 Frequency ratio consistency loss

This loss constrains that the frequency ratio between any positive and negative rPPG signals ( $\mathbf{y}^p$  and  $\mathbf{y}^n$ ) should be consistent with the corresponding ratio  $r$  fed into the LFA module. We define the frequency ratio consistency loss  $\mathcal{L}_{fr}$ :

$$\mathcal{L}_{fr} = \frac{1}{2k} \sum_{i=1}^k \left| \frac{P(\mathbf{y}_i^n)}{P(\mathbf{y}_1^p)} - r_i \right| + \left| \frac{P(\mathbf{y}_i^n)}{P(\mathbf{y}_2^p)} - r_i \right| \quad (4)$$

where we use  $P(\cdot)$  to measure a signal’s dominant frequency.  $P$  is implemented by following [13] to apply fast Fourier transform on a given signal and select the frequency component with maximum power.  $\mathbf{y}_1^p$  and  $\mathbf{y}_2^p$  should ideally have the same frequency.  $\frac{P(\mathbf{y}_i^n)}{P(\mathbf{y}_1^p)}$  indicates the dominant frequency ratio between signal  $\mathbf{y}_i^n$  and  $\mathbf{y}_1^p$ . If this ratio is equal to  $r_i$ , that means the LFA module has successfully generated  $\mathbf{x}_i^n$  with the target rPPG signal frequency  $r_i \times f^a$ .

#### 3.4.3 Cross-video frequency agreement loss

This loss function is built upon the observation that the frequency of a rPPG signal does not change rapidly over a short term. Based on this, the rPPG signal from the input  $\mathbf{x}^a$  should have a similar frequency to those from  $\mathbf{x}^a$ ’s temporal neighbors (see Sec. 3.1). We pass  $\mathbf{x}^a$ ’s neighboring video clips through REA modules to extract rPPG signals from them, *i.e.*  $\mathbf{Y}^b = \{\mathbf{y}^b\}$ . We design the cross-video frequency agreement loss  $\mathcal{L}_{fa}$  to enforce the frequency conformability between  $\mathbf{Y}^p$  and  $\mathbf{Y}^b$ :

$$\mathcal{L}_{fa} = \frac{1}{2J} \sum_{j=1}^J d(\mathbf{y}_1^p, \mathbf{y}_j^b) + d(\mathbf{y}_2^p, \mathbf{y}_j^b) \quad (5)$$

where  $d(\cdot, \cdot)$  is the same to that in Eqn. 3. We have  $J$  neighbors in total. This loss helps reduce the signal estimation error and improve the signal periodicity.

The overall loss function is a linear combination of the above frequency-inspired losses as well as the video reconstruction loss in Sec. 3.2.2:

$$\mathcal{L} = \mathcal{L}_{fc} + \mathcal{L}_{fr} + \mathcal{L}_{fa} + \mathcal{L}_{vr} \quad (6)$$

## 4 EXPERIMENTS

### 4.1 Datasets

We conduct our experiments on four public datasets: UBFC-rPPG [20], PURE [21], DEAP [22], and MMVS [3].

**UBFC-rPPG** consists of 42 face videos with simultaneously recorded PPG signals and heart rates. The resolution and frame rate of each face video is  $640 \times 480$  and 30 frames per second (FPS), respectively. We follow [4] to discard subjects of indices 11, 18, 20 and 24 because their heart rates were inappropriately recorded.

**PURE** contains 60 face videos from 10 subjects. During the data collection process, subjects were asked to perform six kinds of head motions (small rotation, medium rotation, slow translation, fast translation, talking and steady) in front of the camera for one minute. The videos were captured at a frame rate of 30 FPS and a resolution of  $640 \times 480$ . The ground truth PPG signals were recorded using a finger clip pulse oximeter with a sampling rate of 60 Hz. We follow [19] to discard the first two samples because their PPG wave forms were strongly corrupted.

**DEAP** consists of 874 face videos associated with multi-channel physiological signals. They were taken from 22 subjects by playing one-minute musical excerpts to them. Each video has a resolution of  $720 \times 576$  and a frame rate of 50 FPS.

**MMVS** contains 745 face videos from 129 subjects. A depth camera and a finger clip pulse oximeter was utilized to

TABLE 1

Comparison to state of the art on HR estimation. The results are reported on UBFC-rPPG, PURE, DEAP and MMVS datasets.  $\uparrow$  indicates that the larger the value is the better it is and  $\downarrow$  vice versa. The best supervised approach is marked in **shadow**, while the best self-supervised approach is marked in **bold**.

Method	PPG annotations	UBFC-rPPG			PURE			DEAP			MMVS		
		MAE $\downarrow$	RMSE $\downarrow$	$r$ $\uparrow$	MAE $\downarrow$	RMSE $\downarrow$	$r$ $\uparrow$	MAE $\downarrow$	RMSE $\downarrow$	$r$ $\uparrow$	MAE $\downarrow$	RMSE $\downarrow$	$r$ $\uparrow$
POS [10]	-	8.35	10.00	0.24	3.14	10.57	0.95	7.39	10.25	0.82	6.77	9.40	0.82
CHROM [14]	-	8.20	9.92	0.27	3.82	6.80	0.97	7.47	10.31	0.82	6.85	9.37	0.82
Green [51]	-	6.01	7.87	0.29	4.39	11.60	0.90	8.10	11.17	0.80	7.13	9.46	0.80
SynRhythm [52]	$\checkmark$	5.59	6.82	0.72	2.71	4.86	0.98	5.08	5.92	0.87	4.48	6.52	0.89
Meta-rppg [4]	$\checkmark$	5.97	7.42	0.53	2.52	4.63	0.98	5.16	6.00	0.87	4.30	6.20	0.91
PulseGan [15]	$\checkmark$	1.19	2.10	0.98	2.28	4.29	0.99	4.86	5.70	0.88	3.52	5.09	0.93
Dual-Gan [5]	$\checkmark$	0.44	<b>0.67</b>	0.99	<b>0.82</b>	<b>1.31</b>	<b>0.99</b>	3.25	4.11	0.91	<b>3.00</b>	<b>4.27</b>	<b>0.94</b>
Physformer [25]	$\checkmark$	<b>0.40</b>	0.71	<b>0.99</b>	1.10	1.75	0.99	<b>3.03</b>	<b>3.96</b>	<b>0.92</b>	3.28	4.50	0.93
Gideon <i>et al.</i> [19]	$\times$	1.85	4.28	0.93	2.32	2.97	0.99	5.13	6.16	0.86	3.43	4.74	0.93
Ours	$\times$	<b>0.58</b>	<b>0.94</b>	<b>0.99</b>	<b>1.23</b>	<b>2.01</b>	<b>0.99</b>	<b>4.20</b>	<b>5.18</b>	<b>0.90</b>	<b>2.93</b>	<b>4.16</b>	<b>0.94</b>

record face videos and PPG signals, respectively. The resolution of each captured video is  $1920 \times 1080$  and the frame rate is 25 FPS. The sampling rate for PPG signals is 60 Hz.

## 4.2 Implementation Details

For all face videos in four datasets, we follow [19] to use the open-source face detector S3FD [53] to detect and crop the face area in each frame. We randomly sample consecutive 600 frames from each video and follow [19] to scale them into a resolution of  $64 \times 64$  for training. We cut the 600-frame video into four clips, each with equivalent length  $T$  of 150 frames. In every iteration, we randomly select one clip as the main input  $\mathbf{x}^a$  while the rest three ( $J = 3$  in Eqn. 5) are its neighbors. The number of negative samples,  $k$ , is set to 4. The number of face regions,  $L$ , is set to 9. Following [35], the temperature  $\tau$  in Eqn. 3 is set to 0.08. Our model is trained for 100 epochs on four NVIDIA GeForce RTX 2080 GPUs using Pytorch 1.8.0. We use the Adam [54] optimizer and set the batch size to 4. The learning rate is initialized as  $1 \times 10^{-5}$  and is decreased to  $0.5 \times 10^{-5}$  at the 50-th epoch.

## 4.3 Evaluation Protocol

Previous works calculate the heart rate (HR), heart rate variability (HRV) and respiration frequency (RF) from estimated rPPG signals and compare them to the corresponding ground truth for performance evaluation [5], [15], [16], [18]. We follow them to conduct HR evaluation on all four datasets; HRV and RF evaluation on the UBFC-rPPG dataset. Moreover, we perform cross-dataset HR evaluation among UBFC-rPPG, PURE and MMVS. The calculation of HR, HRV and RF is via the toolkit HeartPy [55].

We follow [15], [19] to use mean absolute error (MAE), root mean square error (RMSE) and Pearson’s correlation coefficient ( $r$ ) as evaluation metrics for HR. For HRV, we follow [5], [16], [25] to compute its three attributes, *i.e.* low frequency (LF), high frequency (HF), and LF/HF ratio. LF and HF are calculated from the interbeat intervals under low frequency (0.04 to 0.15 Hz) and high frequency (0.15 to 0.4 Hz) bands of the rPPG signal [5], [25]. For each attribute of HRV, we report the standard deviation (Std) of estimation errors, RMSE and  $r$ . Finally, for RF, we also report the Std,

RMSE and  $r$  as per most comparable methods [5], [16], [18]. We follow [3], [5], [16] to perform the 5-fold subject-exclusive cross-validation for all experiments.

## 4.4 Results

### 4.4.1 HR evaluation

We first evaluate the HR estimation on all datasets. Representative approaches include: 1) traditional blind signal separation- and skin reflection model-based ones: POS [10], CHROM [14] and Green [51]; 2) modern DNN-based supervised ones: SynRhythm [52], Meta-rppg [4], PulseGan [15], Dual-Gan [5], Physformer [25]; and 3) a recent DNN-based self-supervised one: Gideon *et al.* [19]. Their results are shown in Table 1.

First, we observe that the performance of traditional approaches [10], [14], [51] is much inferior to DNN-based ones. DNN-based approaches can be trained in a data-driven way, while traditional approaches heavily rely on priors, which can not always satisfy. Second, DNN-based self-supervised approaches ([19] and ours) show comparable performance to many supervised ones, *e.g.* [4], [5], [15], [25], [52].

Our approach outperforms many supervised approaches. For instance, on the MMVS dataset, it even decreases the MAE/RMSE from best performing one Dual-Gan [5] by 0.07/0.11. MMVS is a large-scale dataset in which videos were captured from different scenarios. We reproduce the state of the art on MMVS using their default parameters, which may need to be adjusted on this large-scale dataset. In contrast, our self-supervised model has demonstrated a good generalizability on this dataset.

Our model also significantly outperforms the very recent self-supervised approach Gideon *et al.* [19] on all four datasets; for example, on UBFC-rPPG, it decreases MAE by 1.27 and RMSE by 3.34. This justifies the effectiveness of our proposed modules and losses.

Fig. 5 shows the Bland-Altman plot and scatter plot on the MMVS dataset.  $HR_{gt}$  and  $HR_{et}$  represent the HR calculated from the ground truth PPG signal and the estimated rPPG signal, respectively. Each point indicates an estimation result from one test sample. The x-axis in the Bland-Altman plot denotes the mean value of  $HR_{gt}$  and  $HR_{et}$

TABLE 2

Comparison to state of the art on RF and HRV estimation. The results are reported on the UBFC-rPPG.  $\uparrow$  indicates that the larger the value is the better it is and  $\downarrow$  vice versa. The best supervised approach is marked in **shadow**, while the best self-supervised approach is marked in **bold**.

Method	UBFC-rPPG	PPG annotations	RF			HRV: LF			HRV: HF			HRV: LF/HF		
			Std $\downarrow$	RMSE $\downarrow$	$r$ $\uparrow$	Std $\downarrow$	RMSE $\downarrow$	$r$ $\uparrow$	Std $\downarrow$	RMSE $\downarrow$	$r$ $\uparrow$	Std $\downarrow$	RMSE $\downarrow$	$r$ $\uparrow$
POS [10]	-	-	0.109	0.107	0.087	0.171	0.169	0.479	0.171	0.169	0.479	0.405	0.399	0.518
CHROM [14]	-	-	0.086	0.089	0.102	0.243	0.240	0.159	0.243	0.240	0.159	0.655	0.645	0.266
Green [51]	-	-	0.087	0.086	0.111	0.186	0.186	0.280	0.186	0.186	0.280	0.361	0.365	0.492
CVD [16]	$\checkmark$	$\checkmark$	0.017	0.018	0.252	0.053	0.065	0.740	0.053	0.065	0.740	0.169	0.168	0.812
rPPGNet [18]	$\checkmark$	$\checkmark$	0.030	0.034	0.233	0.071	0.070	0.686	0.071	0.070	0.686	0.212	0.208	0.744
Dual-Gan [5]	$\checkmark$	$\checkmark$	0.010	0.010	0.395	0.034	0.035	0.891	0.034	0.035	0.891	0.131	0.136	0.881
Physformer [25]	$\checkmark$	$\checkmark$	<b>0.009</b>	<b>0.009</b>	<b>0.413</b>	<b>0.030</b>	<b>0.032</b>	<b>0.895</b>	<b>0.030</b>	<b>0.032</b>	<b>0.895</b>	<b>0.126</b>	<b>0.130</b>	<b>0.893</b>
Gideon <i>et al.</i> [19]	$\times$	$\times$	0.061	0.098	0.103	0.091	0.139	0.694	0.091	0.139	0.694	0.525	0.691	0.684
Ours	$\times$	$\times$	<b>0.023</b>	<b>0.028</b>	<b>0.351</b>	<b>0.047</b>	<b>0.062</b>	<b>0.769</b>	<b>0.047</b>	<b>0.062</b>	<b>0.769</b>	<b>0.160</b>	<b>0.164</b>	<b>0.831</b>

TABLE 3

Comparison to state of the art on cross-dataset HR estimation.  $\uparrow$  indicates that the larger the value is the better it is and  $\downarrow$  vice versa. The best supervised approach is marked in **shadow**, while the best self-supervised approach is marked in **bold**.

Method	PPG annotations	MMVS $\rightarrow$ UBFC-rPPG			UBFC-rPPG $\rightarrow$ MMVS			PURE $\rightarrow$ UBFC-rPPG			UBFC-rPPG $\rightarrow$ PURE		
		MAE $\downarrow$	RMSE $\downarrow$	$r$ $\uparrow$	MAE $\downarrow$	RMSE $\downarrow$	$r$ $\uparrow$	MAE $\downarrow$	RMSE $\downarrow$	$r$ $\uparrow$	MAE $\downarrow$	RMSE $\downarrow$	$r$ $\uparrow$
Meta-rppg [4]	$\checkmark$	6.48	7.97	0.52	5.69	7.74	0.84	6.11	7.58	0.66	4.00	5.98	0.92
PulseGan [15]	$\checkmark$	2.33	3.62	0.97	4.40	6.35	0.89	2.30	3.50	0.97	3.36	5.11	0.95
Dual-Gan [5]	$\checkmark$	2.00	3.13	0.97	3.51	4.99	0.93	2.03	<b>3.01</b>	0.97	<b>1.81</b>	<b>2.97</b>	<b>0.99</b>
Physformer [25]	$\checkmark$	<b>1.97</b>	<b>3.08</b>	<b>0.97</b>	<b>3.46</b>	<b>4.96</b>	<b>0.93</b>	<b>1.93</b>	3.02	<b>0.97</b>	1.99	3.28	0.99
Gideon <i>et al.</i> [19]	$\times$	2.45	3.71	0.93	3.84	5.31	0.91	2.37	3.51	0.95	2.95	4.60	0.97
Ours	$\times$	<b>2.24</b>	<b>3.40</b>	<b>0.97</b>	<b>3.50</b>	<b>4.95</b>	<b>0.93</b>	<b>2.18</b>	<b>3.20</b>	<b>0.97</b>	<b>2.14</b>	<b>3.37</b>	<b>0.98</b>

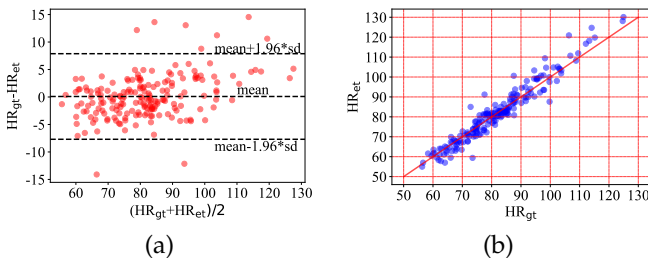


Fig. 5. The Bland-Altman plot (a) and scatter plot (b) show the difference between estimated HR and ground truth HR on the MMVS dataset.

while y-axis represents their difference. The top and bottom dashed lines indicate confidence intervals for 95% limits of agreement. We can observe that  $HR_{gt}$  is well correlated with  $HR_{et}$  within a wide range from 50 bpm to 130 bpm. The Pearson’s correlation coefficient  $r$  between  $HR_{gt}$  and  $HR_{et}$  of our approach is 0.94 (Fig. 5b), which is higher than that of other methods, *e.g.* Meta-rppg [4] (0.91), PulseGan [15] (0.93), Physformer [25] (0.93), Gideon *et al.* [19] (0.93).

#### 4.4.2 RF and HRV evaluation

We further conduct experiments for RF and HRV estimation on the UBFC-rPPG dataset. As mentioned in Sec. 4.3, HRV is represented by its three attributes (LF, HF, LF/HF). Similar to the HR evaluation, we compare our approach with state of the art [5], [10], [14], [16], [18], [19], [25], [51]. The results are shown in Table 2. We can see that our approach outperforms all traditional ones and many deep learning ones. For example, as a self-supervised method, we have a

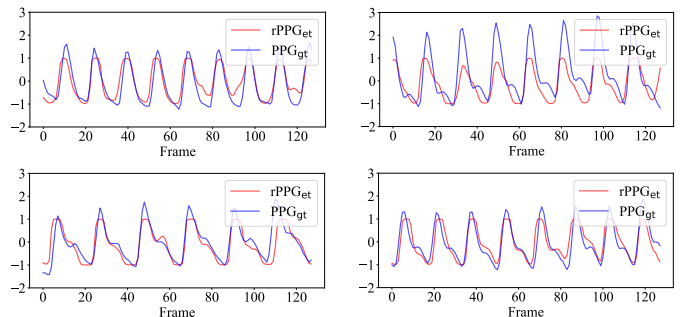


Fig. 6. Four examples for the visual comparison between estimated rPPG signals (red curves) and their corresponding ground truth PPG signals (blue curves).

comparable performance with the very recent supervised method Physformer [25]; moreover, we outperforms the self-supervised competitor [19] by large margins on all metrics.

Fig. 6 shows four estimated rPPG signals and their corresponding ground truth. We can observe that our method predicts rPPG signals with very accurate interbeat intervals compared to ground truth, from which we can obtain robust RF and HRV results.

#### 4.4.3 Cross-dataset HR evaluation

To evaluate the generalizability of our method, we conduct the cross-dataset experiment among UBFC-rPPG, PURE and MMVS datasets and report the HR results in Table 3. Specifically, we train our model, as well as state of the art,



TABLE 4

Ablation study on the frequency modulation block (FMB) and video reconstruction loss in LFA module.

Method	UBFC-rPPG			MMVS		
	MAE↓	RMSE↓	$r \uparrow$	MAE↓	RMSE↓	$r \uparrow$
Ours	<b>0.58</b>	<b>0.94</b>	<b>0.99</b>	<b>2.93</b>	<b>4.16</b>	<b>0.94</b>
Ours w/o LFA	1.27	1.91	0.97	3.21	4.48	0.93
FMB-Linear	1.05	1.71	0.97	3.17	4.46	0.93
FMB w/o 1D RB	0.80	1.30	0.98	3.03	4.39	0.93
FMB w/o BiLSTM	0.72	1.25	0.99	3.00	4.29	0.93
FMB-LSTM	0.66	1.07	0.99	2.98	4.26	0.94
FMB-GRU	0.68	1.06	0.99	2.98	4.26	0.94
FMB-BiGRU	0.60	0.97	0.99	2.93	4.19	0.94
LFA w/o $\mathcal{L}_{vr}$	0.88	1.36	0.98	3.04	4.34	0.94
$\mathcal{L}_{vr} \rightarrow \mathcal{L}_{mr}$	0.69	1.11	0.99	3.02	4.30	0.93

TABLE 5

Ablation study on the multi-scale architecture in LFA module.

Method	UBFC-rPPG			MMVS		
	MAE↓	RMSE↓	$r \uparrow$	MAE↓	RMSE↓	$r \uparrow$
LFA-S1	0.83	1.32	0.98	3.04	4.33	0.94
LFA-S2	0.66	1.06	0.99	2.99	4.24	0.94
LFA-S3	<b>0.58</b>	<b>0.94</b>	<b>0.99</b>	<b>2.93</b>	<b>4.16</b>	<b>0.94</b>
LFA-S4	0.58	0.95	0.99	2.96	<b>4.15</b>	0.94

*i.e.* [4], [5], [15], [19], [25], on one dataset and test them on another. For example, MMVS→UBFC-rPPG means training on MMVS while testing on UBFC-rPPG. Ours and [19] are trained in the self-supervised way while the rest is in the supervised way. We can see that our method produces very competitive results on par with state of the art supervised methods [5], [15], [25]; significantly outperforms the recent self-supervised method [19]. This shows the good generalizability of our method in new (unseen) scenarios.

#### 4.4.4 Ablation Study

We conduct ablation study from five aspects: LFA module, REA module, frequency-inspired losses, temporally neighboring videos and spatial augmentation. The results for HR estimation are reported on UBFC-rPPG and MMVS datasets. **Learnable frequency augmentation (LFA) module.** Table 4 presents the ablation study on the proposed LFA module. First, we use Ours w/o LFA to indicate the variant without using LFA module; instead, we follow [19] to manually change the frame rate of the input video and generate only one negative sample for self-supervised learning. We can observe severe performance degradation by this variant on each metric, which justifies the advantage of LFA module for obtaining negative samples with more diverse rPPG signal frequencies.

**Multi-scale in LFA:** the LFA module performs frequency transformation on three scales (S3). We also experiment with one scale (S1), two scales (S2) and four scales (S4) in Table 5. They are denoted as LFA-S1, LFA-S2, LFA-S3 and LFA-S4, respectively. We can observe that LFA-S3 performs in general the best. LFA-S4 performs very close to LFA-S3 yet with additional computations. LFA-S1/S2 performs clearly inferior to LFA-S3. Overall, the three-scale version appears

TABLE 6

Ablation study on different number of negative samples in LFA module.

Method	UBFC-rPPG			MMVS		
	MAE↓	RMSE↓	$r \uparrow$	MAE↓	RMSE↓	$r \uparrow$
Ours ( $k = 1$ )	1.10	1.87	0.97	3.10	4.28	0.93
Ours ( $k = 2$ )	1.03	1.66	0.97	3.07	4.35	0.94
Ours ( $k = 3$ )	0.75	1.27	0.98	3.00	4.23	0.94
Ours ( $k = 4$ )	<b>0.58</b>	<b>0.94</b>	<b>0.99</b>	<b>2.93</b>	4.16	<b>0.94</b>
Ours ( $k = 5$ )	0.58	0.96	0.99	2.93	<b>4.15</b>	0.94

TABLE 7

Ablation study on the proposed REA module.

Method	UBFC-rPPG			MMVS		
	MAE↓	RMSE↓	$r \uparrow$	MAE↓	RMSE↓	$r \uparrow$
Ours	<b>0.58</b>	<b>0.94</b>	<b>0.99</b>	<b>2.93</b>	<b>4.16</b>	<b>0.94</b>
REA→GRA	1.16	1.85	0.97	3.29	4.61	0.93
REA w/o RA	1.02	1.69	0.97	3.13	4.40	0.93
RA→SA	0.62	0.95	0.99	2.96	4.22	0.94
$\mathcal{G} \rightarrow \text{avg}$	1.12	1.89	0.97	3.23	4.56	0.93
$\mathcal{G} \rightarrow \mathcal{G}_{spat}$	0.76	1.26	0.98	3.07	4.41	0.94

to be sufficient to describe different levels of details for the input. This is our default setting.

**Feature modulation block in LFA:** we further verify the design of the feature modulation block (FMB) in the LFA module. As mentioned in Sec. 3.2.1, the key part of FMB is the 1D RB and BiLSTM for non-linear signal frequency transformation. A linear transformation here is not adequate. For instance, we can replace 1D RB + BiLSTM by three 1D Convs, which we call it FMB-Linear in Table 4. We see that the performance drops substantially by FMB-Linear, attesting that non-linear functions are important for frequency transformation.

Furthermore, we use FMB w/o 1D RB and FMB w/o BiLSTM to denote the FMB without 1D RB or BiLSTM. We can observe that both 1D RB and BiLSTM contribute to the final result. 1D RB is responsible for signal’s local transformation followed by non-linear activation function, ReLU. BiLSTM dedicates to signal’s global transformation along the temporal dimension. Alternatively, we can replace BiLSTM with other RNN units, such as LSTM, GRU and BiGRU. We name these variants as FMB-LSTM, FMB-GRU and FMB-BiGRU in Table 4: they show competitive performance but our FMB with BiLSTM is the best.

**Video reconstruction loss in LFA:** We utilize video reconstruction loss  $\mathcal{L}_{vr}$  to reduce color differences between negative samples and the original sample. If we remove  $\mathcal{L}_{vr}$ , the result (LFA w/o  $\mathcal{L}_{vr}$  in Table 4) will be much inferior. As mentioned in Sec. 3.2.2, an alternative to  $\mathcal{L}_{vr}$  is to regulate the modulation vector, *i.e.*  $\mathcal{L}_{mr} = \frac{1}{k} \sum_{i=1}^k \|\mathbf{m}_i - 1\|_2$ . We report the result for this variant in Table 4:  $\mathcal{L}_{vr} \rightarrow \mathcal{L}_{mr}$ , it works by improving upon LFA w/o  $\mathcal{L}_{vr}$  yet is no better than Ours with  $\mathcal{L}_{vr}$ .

**Number of negative samples in LFA:** In the training phase, we found that the number of negative samples affects the model performance. We vary this number  $k$  from 1 to 6 and report the result in Table 6. Our default setting ( $k = 4$ ) appears to be the best.

TABLE 8  
Ablation study on the number of experts in REA module.

Method	UBFC-rPPG			MMVS		
	MAE↓	RMSE↓	$r$ ↑	MAE↓	RMSE↓	$r$ ↑
Ours ( $L = 2$ )	0.75	1.15	0.98	3.17	4.48	0.93
Ours ( $L = 4$ )	0.61	0.98	0.99	2.97	4.19	0.94
Ours ( $L = 9$ )	0.58	<b>0.94</b>	<b>0.99</b>	<b>2.93</b>	<b>4.16</b>	<b>0.94</b>
Ours ( $L = 16$ )	<b>0.57</b>	0.94	0.99	2.95	4.16	0.94
Ours ( $L = 25$ )	0.58	0.95	0.99	2.94	4.18	0.94

**Local rPPG expert aggregation (REA) module.** We investigate the effectiveness of the REA module in Table 7. The first variant is to not use the local rPPG experts but simply extract the rPPG signal from the entire face. The REA module degrades to one 3D ResNet-10 block at the beginning followed by one 3D GAP and one 1D Conv for rPPG estimation. We denote this variant as a global rPPG estimation (GRA) module, *i.e.* REA→GRA, in Table 7. We can observe that the MAE increases by 0.58 and the RMSE increases by 0.91 on UBFC-rPPG. This shows that encoding complementary pulsation information from different face regions helps improve the rPPG estimation. Below we study the importance of the region-attention (RA) block and spatio-temporal gating net in the REA module.

*Region-attention block in REA:* Referring to Fig. 4b, we can replace the RA block with a 3D RB in the REA module. We denote this by REA w/o RA in Table 7: the MAE increases to 1.02, RMSE increases to 1.69, and  $r$  decreases to 0.97 on the UBFC-rPPG dataset. The proposed RA block is more effective than a simple 3D RB in finding the pulsation-sensitive area in a region. Alternatively, we follow [18] to use an additional skin segmentation branch after the 3D ResNet-10 block. This branch produces a seg-attention (SA) map, which we use to replace the region-attention map and is multiplied back to the encoded feature. We denote this by RA→SA. It performs better than REA w/o RA but is still inferior to RA. SA map assigns weights to pixels according to their likelihood of being face skins; our RA map instead assigns weights to pixels according to their sensitivities to pulsation changes. RA can capture more discriminative physiological clues from face skins for rPPG estimation.

*Spatio-temporal gating net in REA:* The spatio-temporal gating net  $\mathcal{G}$  assigns weights to local rPPG experts for their aggregation. If we remove it from the REA module but takes the average of multiple experts, the MAE and RMSE will be significantly increased for HR estimation (see Table 7:  $\mathcal{G} \rightarrow avg$ ). This supports our claim that the distribution of blood vessels varies over face regions. Our gating net treats these regions differently in rPPG estimation. Next, we adjust  $\mathcal{G}$  to assign one scalar weight to one expert (corresponding to a spatial region) while ignoring the temporal change in the signal. We denote this by  $\mathcal{G} \rightarrow \mathcal{G}_{spat}$  in Table 7: one can clearly see the performance drop by this variant. This validates our motivation that each expert signal should be assigned with different weights at different moments (see Sec. 3.3.2).

*Number of experts in REA:* We vary the number of local rPPG experts  $L$  from 2, 4 ( $2 \times 2$ ), 9 ( $3 \times 3$ ), 16 ( $4 \times 4$ ), and 25 ( $5 \times 5$ ) in the REA module and show the performance in

TABLE 9  
Ablation study on the frequency-inspired losses.

Method	UBFC-rPPG			MMVS		
	MAE↓	RMSE↓	$r$ ↑	MAE↓	RMSE↓	$r$ ↑
Ours	0.58	<b>0.94</b>	<b>0.99</b>	<b>2.93</b>	4.16	<b>0.94</b>
Ours w/o $\mathcal{L}_{fc}$	2.13	3.09	0.83	5.00	6.74	0.85
Ours w/o $\mathcal{L}_{fr}$	0.89	1.39	0.98	3.07	4.35	0.94
Ours w/o $\mathcal{L}_{fa}$	0.67	1.08	0.99	3.04	4.30	0.94
$\mathcal{L}_{fr} \rightarrow \mathcal{L}_{fr-single}$	0.66	1.08	0.99	3.00	4.24	0.94
$\mathcal{L}_{fa} \rightarrow \mathcal{L}_{fa-single}$	0.60	0.98	0.99	3.00	4.26	0.94
Ours-expand	<b>0.55</b>	0.96	0.99	2.94	<b>4.14</b>	0.94

Table 8. Our default setting ( $L = 9$ ) appears to be the best. Yet, the performance difference for  $L$  from 4 to 25 is not big. **Frequency-inspired losses.** To validate the effectiveness of our proposed frequency contrastive loss  $\mathcal{L}_{fc}$ , frequency ratio consistency loss  $\mathcal{L}_{fr}$ , cross-video frequency agreement loss  $\mathcal{L}_{fa}$ , we ablate them one by one in our framework and show the results in Table 9. We observe clear performance drop by removing any of them.

*Frequency contrastive loss  $\mathcal{L}_{fc}$ :* Without using  $\mathcal{L}_{fc}$ , the MAE and RMSE for HR evaluation are substantially increased while the  $r$  is substantially decreased, *e.g.* 5.00, 6.74 and 0.85 on MMVS.  $\mathcal{L}_{fc}$  enforces the signal frequency similarities among positive samples and dissimilarities between positive and negative samples. It optimizes the model embedding space to be discriminative to skin color changes.

*Frequency ratio consistency loss  $\mathcal{L}_{fr}$ :* Without  $\mathcal{L}_{fr}$ , the result also gets worse on both UBFC-rPPG and MMVS datasets.  $\mathcal{L}_{fr}$  consists of two terms corresponding to the two positive signals,  $\mathbf{y}_1^p$  and  $\mathbf{y}_2^p$ , which should ideally share the same frequency. Nonetheless, we argue that in practice both  $\mathbf{y}_1^p$  and  $\mathbf{y}_2^p$  are important in Eqn.4. We offer a variant by keeping only the first term in Eqn.4 and name it as  $\mathcal{L}_{fr} \rightarrow \mathcal{L}_{fr-single}$  in Table 9. This shows inferior performance compared to the original  $\mathcal{L}_{fr}$  (Ours). Having both terms in Eqn.4 can implicitly pull the two positive signals close.

*Cross-video frequency agreement loss  $\mathcal{L}_{fa}$ :* We conduct similar experiment to that of  $\mathcal{L}_{fr}$  by removing  $\mathcal{L}_{fa}$ , where clear performance drop can be observed on both datasets. Next, we offer a variant of  $\mathcal{L}_{fa}$  by keeping only its first term in Eqn.5. We denote this by  $\mathcal{L}_{fa} \rightarrow \mathcal{L}_{fa-single}$  in Table 9. The result also gets worse which further validates the importance of having both positive signals.

**Temporally neighboring videos.** Given a short term face video, we cut it into  $J + 1$  clips, each with  $T$  frames, and randomly select one as the main input  $\mathbf{x}^a$ . In this session, we study the attributes of these temporal neighbors.

*Augmentation:* we notice that for  $\mathbf{x}^a$ 's neighbors, they are only applied with the loss  $\mathcal{L}_{fa}$ , but are not augmented and applied with other losses ( $\mathcal{L}_{fc}$ ,  $\mathcal{L}_{fr}$ ,  $\mathcal{L}_{vr}$ ). This is because the rPPG signals among neighboring video clips are very similar, there is no need to repeat the augmentation process to every one of them. To support our claim, we apply all loss terms to both  $\mathbf{x}^a$  and its neighbors, and denote this by Ours-expand in Table 9. Only slight improvement can be observed by comparing it to Ours. Considering the computation increase, we do not recommend it.

*Length of one video clip:* We vary the length of each video

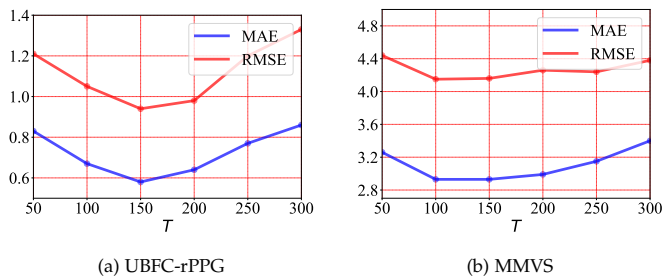


Fig. 7. Parameter variation on the length of one video clip.

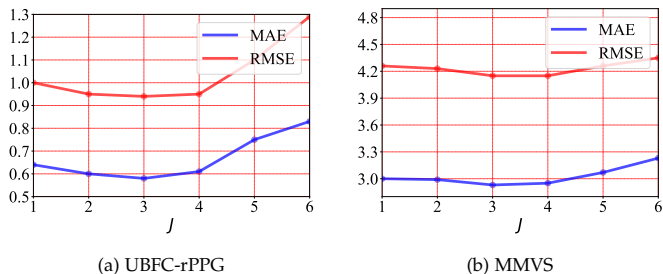


Fig. 8. Parameter variation on the number of video clips.

TABLE 10  
Ablation study on spatial augmentation.

Method	UBFC-rPPG			MMVS		
	MAE $\downarrow$	RMSE $\downarrow$	$r \uparrow$	MAE $\downarrow$	RMSE $\downarrow$	$r \uparrow$
Ours ( $p = 1$ )	0.62	1.00	0.99	2.95	4.20	0.94
Ours ( $p = 2$ )	0.58	<b>0.94</b>	<b>0.99</b>	<b>2.93</b>	4.16	<b>0.94</b>
Ours ( $p = 3$ )	0.58	0.95	0.99	2.93	<b>4.15</b>	0.94
Ours ( $p = 4$ )	<b>0.56</b>	0.96	0.99	2.94	4.16	0.94
Ours-CJ	7.33	8.97	0.20	8.29	10.98	0.47
Ours-SF	7.59	9.55	0.19	8.33	10.70	0.46

clip  $T$  from 50, 100, 150, 200, 250, and 300 in Fig. 7. The number of video clips is fixed to 4 ( $J = 3$ ). We only draw the MSE and RMSE result on HR estimation; the change for Pearson coefficient  $r$  is insignificant. We can observe that  $T = 150$  appears to be the best on UBFC-rPPG. The performance on MMVS is rather stable by varying  $T$  between 100 and 200. In general, we argue that  $T$  should not be too big; otherwise, the signals from temporal neighbors would not be similar.

*Number of video clips:* We can also vary the number of video clips while fixing the length of one clip to 150. We vary  $J$  from 1 to 6 in Fig. 8. We can see the performance is stable on both datasets between  $J = 1$  and 4. Similar to  $T$ ,  $J$  should also not be too big such that neighboring signals remain to be similar. Our default  $J$  is 3.

**Spatial Augmentation.** We investigate the number of spatially augmented samples and the type of spatial augmentation.

*The number of spatially augmented samples:* We vary the number of positive (spatially augmented) samples from  $p = 1$  to  $p = 4$  in Table 10. When the number is 2, it appears to be a good trade-off between accuracy and computation. This is also our default setting. Notice that [19] only generates one positive sample by applying inverse transformation on the negative one, which is fundamentally different from our spatial augmentation.

*The type of spatial augmentation:* The weakly spatial augmentation we adopt includes image rotation and flip. We choose them because they do not alter the color change across frames, thus do not affect the rPPG signal contained in videos. There exist many other types of spatial augmentation, e.g. color jittering and Sobel filtering. They are however not suitable for our task, as they clearly alter the color distribution across frames, so as to change the underlying signal frequencies in videos. To validate this, we offer two variants, denoted by Ours-CJ and Ours-SF, in Table 10. For each variant, we generate two positive samples, one is the original input, the other is with color jittering or Sobel filtering. Both variants show very poor performance.

## 5 CONCLUSION

In this paper, we propose a new frequency-inspired self-supervised framework for video-based remote physiological measurement. Our approach consists of three key stages: data augmentation, signal extraction and network optimization. For data augmentation, we randomly select a video clip from a given face video as the main input. We introduce the LFA module to generate sufficient negative samples from it. These negative samples contain rPPG signals with different frequencies to the input. Meanwhile, we also apply spatial augmentation on the input to obtain positive samples that share the same rPPG signal frequency to that of the input. For signal extraction, we design the REA module to extract complementary physiological clues from different face regions and aggregate them for an accurate rPPG estimation. In the REA module, a region-attention block is devised to focus the estimation on pulsation-sensitive skins and a spatio-temporal gating net is devised to combine temporal signals over different spatial regions. Last, for the network optimization, we propose a series of frequency-inspired losses to optimize estimated rPPG signals from the input’s augmentations and neighbors. Experiments on four datasets show the effectiveness and superiority of our method over state of the art.

## REFERENCES

- [1] X. Niu, S. Shan, H. Han, and X. Chen, “RhythmNet: End-to-End Heart Rate Estimation From Face via Spatial-Temporal Representation,” *IEEE Transactions on Image Processing*, vol. 29, pp. 2409–2423, 2020.
- [2] Y. Qiu, Y. Liu, J. Arteaga-Falconi, H. Dong, and A. El Saddik, “EVM-CNN: Real-Time Contactless Heart Rate Estimation From Facial Video,” *IEEE Transactions on Multimedia*, vol. 21, no. 7, pp. 1778–1787, 2019.
- [3] Z. Yue, S. Ding, S. Yang, H. Yang, Z. Li, Y. Zhang, and Y. Li, “Deep Super-Resolution Network for rPPG Information Recovery and Noncontact Heart Rate Estimation,” *IEEE Transactions on Instrumentation and Measurement*, vol. 70, pp. 1–11, 2021.
- [4] E. Lee, E. Chen, and C.-Y. Lee, “Meta-rPPG: Remote Heart Rate Estimation Using a Transductive Meta-learner,” in *ECCV*, 2020.
- [5] H. Lu, H. Han, and S. K. Zhou, “Dual-GAN: Joint BVP and Noise Modeling for Remote Physiological Measurement,” in *CVPR*, 2021.
- [6] X. Chen, J. Cheng, R. Song, Y. Liu, R. Ward, and Z. J. Wang, “Video-Based Heart Rate Measurement: Recent Advances and Future Prospects,” *IEEE Transactions on Instrumentation and Measurement*, vol. 68, no. 10, pp. 3600–3615, 2019.
- [7] B. P. Yan, W. H. S. Lai, C. K. Y. Chan, A. C. K. Au, B. Freedman, Y. C. Poh, and M.-Z. Poh, “High-Throughput, Contact-Free Detection of Atrial Fibrillation From Video With Deep Learning,” *JAMA Cardiology*, vol. 5, no. 1, p. 105, 2020.

- [8] X. Liu, X. Yang, D. Wang, A. Wong, L. Ma, and L. Li, "VidAF: A Motion-Robust Model for Atrial Fibrillation Screening From Facial Videos," *IEEE Journal of Biomedical and Health Informatics*, vol. 26, no. 4, pp. 1672–1683, 2022.
- [9] E. M. Nowara, T. K. Marks, H. Mansour, and A. Veeraraghavan, "SparsePPG: Towards Driver Monitoring Using Camera-Based Vital Signs Estimation in Near-Infrared," in *CVPR Workshops*, 2018.
- [10] W. Wang, A. C. den Brinker, S. Stuijk, and G. de Haan, "Algorithmic Principles of Remote PPG," *IEEE Transactions on Biomedical Engineering*, vol. 64, no. 7, pp. 1479–1491, 2017.
- [11] Z. Yue, S. Ding, S. Yang, L. Wang, and Y. Li, "Multimodal Information Fusion Approach for Noncontact Heart Rate Estimation Using Facial Videos and Graph Convolutional Network," *IEEE Transactions on Instrumentation and Measurement*, vol. 71, pp. 1–13, 2022.
- [12] M.-Z. Poh, D. J. McDuff, and R. W. Picard, "Advancements in Noncontact, Multiparameter Physiological Measurements Using a Webcam," *IEEE Transactions on Biomedical Engineering*, vol. 58, no. 1, pp. 7–11, 2011.
- [13] M.-Z. Poh and D. J. McDuff, "Non-contact, automated cardiac pulse measurements using video imaging and blind source separation," *Optics Express*, vol. 18, no. 10, p. 10762, 2010.
- [14] G. de Haan and V. Jeanne, "Robust Pulse Rate From Chrominance-Based rPPG," *IEEE Transactions on Biomedical Engineering*, vol. 60, no. 10, pp. 2878–2886, 2013.
- [15] R. Song, H. Chen, J. Cheng, C. Li, Y. Liu, and X. Chen, "PulseGAN: Learning to Generate Realistic Pulse Waveforms in Remote Photoplethysmography," *IEEE Journal of Biomedical and Health Informatics*, vol. 25, no. 5, pp. 1373–1384, 2021.
- [16] X. Niu, Z. Yu, H. Han, X. Li, S. Shan, and G. Zhao, "Video-Based Remote Physiological Measurement via Cross-Verified Feature Disentangling," in *ECCV*, 2020.
- [17] K. He, X. Zhang, S. Ren, and J. Sun, "Deep Residual Learning for Image Recognition," in *CVPR*, 2016.
- [18] Z. Yu, W. Peng, X. Li, X. Hong, and G. Zhao, "Remote Heart Rate Measurement From Highly Compressed Facial Videos: An End-to-End Deep Learning Solution With Video Enhancement," in *ICCV*, 2019.
- [19] J. Gideon and S. Stent, "The Way to my Heart is through Contrastive Learning: Remote Photoplethysmography from Unlabelled Video," in *ICCV*, 2021.
- [20] S. Bobbia, R. Macwan, Y. Benezeth, A. Mansouri, and J. Dubois, "Unsupervised skin tissue segmentation for remote photoplethysmography," *Pattern Recognition Letters*, vol. 124, pp. 82–90, 2019.
- [21] R. Stricker, S. Muller, and H.-M. Gross, "Non-contact video-based pulse rate measurement on a mobile service robot," in *IEEE International Symposium on Robot and Human Interactive Communication*, 2014.
- [22] S. Koelstra, C. Muhl, M. Soleymani, Jong-Seok Lee, A. Yazdani, T. Ebrahimi, T. Pun, A. Nijholt, and I. Patras, "DEAP: A Database for Emotion Analysis Using Physiological Signals," *IEEE Transactions on Affective Computing*, vol. 3, no. 1, pp. 18–31, 2012.
- [23] A. Lam and Y. Kuno, "Robust Heart Rate Measurement from Video Using Select Random Patches," in *ICCV*, 2015.
- [24] R. Macwan, Y. Benezeth, and A. Mansouri, "Heart rate estimation using remote photoplethysmography with multi-objective optimization," *Biomedical Signal Processing and Control*, vol. 49, pp. 24–33, 2019.
- [25] Z. Yu, Y. Shen, J. Shi, H. Zhao, P. H. S. Torr, and G. Zhao, "PhysFormer: Facial Video-Based Physiological Measurement With Temporal Difference Transformer," in *CVPR*, 2022.
- [26] M. Hu, F. Qian, D. Guo, X. Wang, L. He, and F. Ren, "ETA-rPPGNet: Effective Time-Domain Attention Network for Remote Heart Rate Measurement," *IEEE Transactions on Instrumentation and Measurement*, vol. 70, pp. 1–12, 2021.
- [27] M. Noroozi and P. Favaro, "Unsupervised Learning of Visual Representations by Solving Jigsaw Puzzles," in *ECCV*, 2016.
- [28] S. Gidaris, P. Singh, and N. Komodakis, "Unsupervised Representation Learning by Predicting Image Rotations," in *ICLR*, 2018.
- [29] M. Noroozi, H. Pirsiavash, and P. Favaro, "Representation Learning by Learning to Count," in *ICCV*, 2017.
- [30] C. Vondrick, H. Pirsiavash, and A. Torralba, "Anticipating Visual Representations from Unlabeled Video," in *CVPR*, 2016.
- [31] X. Wang and A. Gupta, "Unsupervised Learning of Visual Representations Using Videos," in *ICCV*, 2015.
- [32] K. He, H. Fan, Y. Wu, S. Xie, and R. Girshick, "Momentum Contrast for Unsupervised Visual Representation Learning," in *CVPR*, 2020.
- [33] X. Chen and K. He, "Exploring Simple Siamese Representation Learning," in *CVPR*, 2021.
- [34] T. Chen, S. Kornblith, M. Norouzi, and G. Hinton, "A Simple Framework for Contrastive Learning of Visual Representations," in *ICML*, 2020.
- [35] A. Diba, V. Sharma, R. Safdari, D. Lotfi, M. S. Sarfraz, R. Stiefelhagen, and L. Van Gool, "Vi2CLR: Video and Image for Visual Contrastive Learning of Representation," in *ICCV*, 2021.
- [36] X. Wang and G.-J. Qi, "Contrastive Learning with Stronger Augmentations," *IEEE Transactions on Pattern Analysis and Machine Intelligence*, pp. 1–12, 2022.
- [37] H. Xu, H. Xiong, and G.-J. Qi, "K-Shot Contrastive Learning of Visual Features with Multiple Instance Augmentations," *IEEE Transactions on Pattern Analysis and Machine Intelligence*, 2021.
- [38] R. Dangovski, L. Jing, C. Loh, S. Han, A. Srivastava, B. Cheung, P. Agrawal, and M. Soljačić, "Equivariant Contrastive Learning," in *ICLR*, 2022.
- [39] R. Qian, T. Meng, B. Gong, M.-H. Yang, H. Wang, S. Belongie, and Y. Cui, "Spatiotemporal Contrastive Video Representation Learning," in *CVPR*, 2021.
- [40] T. Pan, Y. Song, T. Yang, W. Jiang, and W. Liu, "VideoMoCo: Contrastive Video Representation Learning with Temporally Adversarial Examples," in *CVPR*, 2021.
- [41] R. A. Jacobs, M. I. Jordan, S. J. Nowlan, and G. E. Hinton, "Adaptive Mixtures of Local Experts," *Neural Computation*, vol. 3, no. 1, pp. 79–87, 1991.
- [42] A. Srivastava, R. Su, and A. Weigend, "Data mining for features using scale-sensitive gated experts," *IEEE Transactions on Pattern Analysis and Machine Intelligence*, vol. 21, no. 12, pp. 1268–1279, 1999.
- [43] M. Emad, M. Peemen, and H. Corporaal, "MoESR: Blind Super-Resolution using Kernel-Aware Mixture of Experts," in *WACV*, 2022.
- [44] Y. Shi, B. Paige, P. Torr *et al.*, "Variational mixture-of-experts autoencoders for multi-modal deep generative models," in *NIPS*, 2019.
- [45] J. Ma, Z. Zhao, X. Yi, J. Chen, L. Hong, and E. H. Chi, "Modeling Task Relationships in Multi-task Learning with Multi-gate Mixture-of-Experts," in *ACM SIGKDD*, 2018.
- [46] M. Sahasrabudhe, P. Sujobert, E. I. Zacharaki, E. Maurin, B. Grange, L. Jallades, N. Paragios, and M. Vakalopoulou, "Deep Multi-Instance Learning Using Multi-Modal Data for Diagnosis of Lymphocytosis," *IEEE Journal of Biomedical and Health Informatics*, vol. 25, no. 6, pp. 2125–2136, Jun. 2021.
- [47] R. Szeto, X. Sun, K. Lu, and J. J. Corso, "A Temporally-Aware Interpolation Network for Video Frame Inpainting," *IEEE Transactions on Pattern Analysis and Machine Intelligence*, vol. 42, no. 5, pp. 1053–1068, May 2020.
- [48] Y. Li, P. Jin, F. Yang, C. Liu, M.-H. Yang, and P. Milanfar, "COMISR: Compression-Informed Video Super-Resolution," in *ICCV*, 2021.
- [49] J. Hu, L. Shen, S. Albanie, G. Sun, and E. Wu, "Squeeze-and-Excitation Networks," *IEEE Transactions on Pattern Analysis and Machine Intelligence*, vol. 42, no. 8, pp. 2011–2023, 2020.
- [50] A. v. d. Oord, Y. Li, and O. Vinyals, "Representation Learning with Contrastive Predictive Coding," *arXiv:1807.03748*, 2019.
- [51] W. Verkruyse, L. O. Svaasand, and J. S. Nelson, "Remote plethysmographic imaging using ambient light," *Optics Express*, vol. 16, no. 26, p. 21434, 2008.
- [52] X. Niu, H. Han, S. Shan, and X. Chen, "SynRhythm: Learning a Deep Heart Rate Estimator from General to Specific," in *Proceedings of the International Conference on Pattern Recognition*, 2018.
- [53] S. Zhang, X. Zhu, Z. Lei, H. Shi, X. Wang, and S. Z. Li, "S3FD: Single Shot Scale-Invariant Face Detector," in *ICCV*, 2017.
- [54] D. P. Kingma and J. Ba, "Adam: A Method for Stochastic Optimization," in *ICLR*, 2017.
- [55] P. Van Gent, H. Farah, N. Van Nes, and B. Van Arem, "Analysing Noisy Driver Physiology Real-Time Using Off-the-Shelf Sensors: Heart Rate Analysis Software from the Taking the Fast Lane Project," *Journal of Open Research Software*, vol. 7, no. 1, p. 32, Oct. 2019.